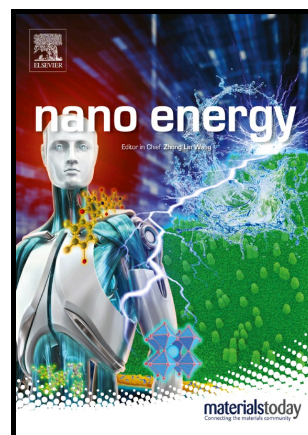


Tracking Lithium Penetration in Solid Electrolyte in 3D by In-situ Synchrotron X-ray Computed Tomography

Shuai Hao, Sohrab R. Daemi, Thomas M.M. Heenan, Wenjia Du, Chun Tan, Malte Storm, Christoph Rau, Dan J.L. Brett, Paul R. Shearing



PII: S2211-2855(21)00003-3

DOI: <https://doi.org/10.1016/j.nanoen.2021.105744>

Reference: NANOEN105744

To appear in: *Nano Energy*

Received date: 7 October 2020

Revised date: 14 December 2020

Accepted date: 3 January 2021

Please cite this article as: Shuai Hao, Sohrab R. Daemi, Thomas M.M. Heenan, Wenjia Du, Chun Tan, Malte Storm, Christoph Rau, Dan J.L. Brett and Paul R. Shearing, Tracking Lithium Penetration in Solid Electrolyte in 3D by In-situ Synchrotron X-ray Computed Tomography, *Nano Energy*, (2020) doi:<https://doi.org/10.1016/j.nanoen.2021.105744>

This is a PDF file of an article that has undergone enhancements after acceptance, such as the addition of a cover page and metadata, and formatting for readability, but it is not yet the definitive version of record. This version will undergo additional copyediting, typesetting and review before it is published in its final form, but we are providing this version to give early visibility of the article. Please note that, during the production process, errors may be discovered which could affect the content, and all legal disclaimers that apply to the journal pertain.

© 2020 Published by Elsevier.

Tracking Lithium Penetration in Solid Electrolyte in 3D by In-situ Synchrotron X-ray Computed Tomography

Shuai Hao^{1,2}, Sohrab R. Daemi¹, Thomas M. M. Heenan^{1,2}, Wenjia Du¹, Chun Tan¹, Malte Storm³, Christoph Rau³, Dan J. L. Brett^{1,2}, Paul R. Shearing^{1,2,*}

¹*Electrochemical Innovation Lab, Department of Chemical Engineering, University College London, London WC1E 7JE, UK*

²*The Faraday Institution, Quad One, Harwell Science and Innovation Campus, Didcot OX11 0RA, UK*

³*Diamond Light Source Ltd, Harwell Science & Innovation Campus, Didcot, Oxfordshire OX11 0DE, United Kingdom*

Corresponding Author: Paul R. Shearing p.shearing@ucl.ac.uk

Abstract

Solid state batteries have attracted extensive attention, but the lithium penetration through the solid electrolyte remains a critical barrier to commercialisation and is not yet fully understood. In this study, the 3D morphological evolution of cracks with deposited lithium were tracked as they penetrated through the solid electrolyte during repetitive plating. This is achieved by utilizing in-situ synchrotron X-ray computed tomography with high spatial and temporal resolutions. Thin-sheet cracks were observed to penetrate the solid electrolyte without immediate short-circuiting of the cell. Changes in their width and volume were quantified. By calculating the volume of deposited lithium, it was found that the lithium was only partially filled in cracks, and its filling ratio quickly dropped from 94.95 % after the 1st plating to ca. 20 % after the 4th plating. The filling process was revealed through tracking the line profile of grayscale along cracks. It was found that lithium grew much more slowly than cracks, so that the cracks near the cathode side were largely hollow and the cell could continue to operate. The deposited lithium after short circuit was segmented and its distribution was visualised. DVC analysis was applied to map local high stress and strain, which aggregated along cracks and significantly increased at areas where new cracks formed.

Key Words

Lithium dendrite; crack; solid electrolyte; in-situ X-ray CT; morphology

Introduction

The increasing demands on commercial lithium-ion batteries in electric vehicles necessitate investigations of new materials and battery systems. Solid state batteries, with lithium metal anodes and solid electrolytes, have been considered as one of the most promising candidates because of their potential in dramatically increasing energy density and safety. Solid electrolytes are non-flammable and were expected to mechanically prevent lithium dendrite penetration¹ which is a pervasive problem when metallic electrodes are used in liquid electrolytes. However, it has been experimentally observed that lithium is able to grow through almost all kinds of solid electrolyte, including oxides^{2,3}, sulphides^{4,5} and polymers⁶⁻⁸, finally causing a short circuit. Various solutions have been proposed to suppress or alleviate dendrites, such as introducing an interface layer⁹⁻¹² and modification of the solid electrolyte^{13,14}. Moreover, the mechanism of lithium dendrite growth has been extensively investigated from both modelling¹⁵⁻¹⁷ and experimental^{5,18-20} perspectives, which in turn could enlighten better solutions.

To fully understand lithium dendrites, characterizing its morphology is of critical importance, but remains challenging. Most characterisation techniques provide only 1D or 2D information of the dendrites, including optical microscopy (OM)^{21,22}, scanning electron microscope (SEM)^{4,5,20,23-25}, nuclear magnetic resonance²⁶, neutron depth profiling^{19,27}. Consequently, the complex three-dimensional morphology cannot be resolved; this is particularly challenging in SSBs where the section 'buried' inside the solid electrolyte is perhaps the most critical. To examine this using conventional microscopy tools, the samples typically have to be disassembled from cells and even broken to expose the internal cross-sections. During these processes, the solid electrolyte (e.g. sulphide) may deteriorate by side-reactions with air^{28,29}, and the delicate lithium dendrites may be disturbed by mechanical force. Focused ion beam microscopy³⁰ can provide a 3D image, however the sample volume is highly limited by the milling efficiency of ion beam typically to ca. tens of microns, which is not large enough to cover the range of a solid electrolyte pellet.

Most of the tests mentioned above are conducted post-mortem, and are unable to track the lithium propagation or the resultant morphological changes in solid electrolytes. With a specially modified cell configuration, in-situ OM^{21,22,30,31} and in-situ SEM^{4,5,20} tests enable real time observation, however, only on the sample surface or at a cross-section. The field of view is seriously limited by the depth of field and the transparency of solid electrolytes.

By contrast, X-ray computed tomography (CT) is a non-destructive test, providing 3D images with high spatial and temporal resolutions. With improvements in spatial resolution achieved over the past decade, X-ray CT has been increasingly applied to study Li-ion batteries³²; however its application in solid state batteries is relatively nascent, the opportunities and challenges of applying this technique to solid state batteries has been summarised by the authors in a recent roadmap³³. Based on the Beer-Lambert law, the image contrast depends on the attenuation difference of the constituent materials³⁴. In solid state batteries, the solid electrolytes usually have a much larger attenuation length compared with the lithium metal, resulting in difficulties in choosing a suitable incident X-ray energy. To address the problem, the cell size should be minimized, meanwhile a solid electrolyte with small X-ray attenuation length is preferred. Obtaining a sufficient temporal resolution to enable in-situ studies requires careful selection of the X-ray source. In the literature, lithium dendrites³⁵ and lithium electrodes^{36,37} in liquid electrolyte systems have been imaged successfully using X-ray CT. In solid state batteries, the lithium electrode was first observed to protrude and grow through polymer electrolytes^{7,38}. For inorganic solid electrolytes, the Li/Li₆PS₅Cl interface evolution was found to gradually result in a loss of contact which was related to the critical current density for dendrite propagation³⁹. Besides, pore structures and distributions inside Li₇La₃Zr₂O₁₂⁴⁰ and Li₁₀GeP₂S₁₂⁴¹ solid electrolytes were clearly imaged by ex-situ tests before and after cycling, and the cracks in Li_{1+x}Al_xGe_{2-x}(PO₄)₃ (LAGP) were observed with their evolution during cycling imaged in-situ⁴²; with coarser resolution compared to the current study commensurate with the use of a laboratory CT scanner. With the coherent and high flux X-ray beam at synchrotron facilities, (for example the Diamond beamline I13^{43,44}), exposure times can be significantly reduced and the image quality is significantly improved, providing a compelling opportunity for dynamic studies. In tandem with high flux sources, bespoke cell configurations have also been developed to maximise image quality and, for example in studies of Li₃PS₄ solid electrolytes⁴⁵. Recently, the electrochemical reduction of Li₁₀GeP₂S₁₂ was observed at the interface with lithium via an

elegant study using synchrotron X-ray CT⁴⁶: as the original solid electrolyte pellet already contained cracks before cycling, elucidating the precise mechanism of crack propagation was challenging. By ensuring a fresh sample in absence of any cracks (to avoid a simple mechanical propagation), the crack initiation and growth that are induced by the lithium deposition during the electrochemical process can be revealed further. X-ray CT is also increasingly being applied to more solid-state batteries systems, including solid-state Li-sulfur⁴⁷ and Sodium batteries⁴⁸⁻⁵⁰, accelerating the development and commercialisation of next generation batteries.

In this study, by utilizing in-situ synchrotron X-ray CT with high spatial and temporal resolution capabilities, the three-dimensional morphological evolution of lithium along with cracks inside a solid electrolyte were tracked during a repetitive plating process until short circuit. The integrity of the solid electrolyte was preserved without any disturbance or movement. The morphologies of cracks were reconstructed in 3D and quantified, and their evolution was statistically analysed through a series of tomograms. Furthermore, the lithium filling process in cracks was analysed and the distribution of deposited lithium after short circuit was segmented. By digital volume correlation (DVC) analysis, the stress and strain was also mapped and analysed.

Result and Discussion

Given the characteristically high X-ray absorption of solid electrolytes, Li₃PS₄ (LPS) was selected as a model solid electrolyte material, considering its smaller X-ray attenuation length (lower X-ray absorption coefficient) than oxide and other sulphide electrolytes (e.g. Li₆PS₅Cl and LAGP), so that the resolution of CT images could be improved further. The ionic conductivity of LPS is comparable to other oxide and polymer electrolytes, although it is not the highest among the sulphide family of candidate materials. However, the lithium penetration process in LPS is representative among a range of solid electrolyte materials. LPS was cold-pressed into a small pellet ca. 2 mm in diameter, and symmetrical Li/LPS/Li cells were assembled into a custom Swagelok battery, as shown in Fig 1a. The battery case, made of polyfluoroalkoxy (PFA), had a chamber of ca. 3 mm in diameter. The cell design has been optimized for X-ray CT with minimal effect on image quality compared with coin cell or pouch cell geometries, as no highly attenuating material is placed in the field of view during tomography⁵¹. The high brilliance synchrotron X-ray source improved image quality, and

dramatically decreased the scan time compared to lab-based alternatives. Optimisation of the material, scanning parameters and cell design all contributed to a high resolution of $0.8 \mu\text{m}$ pixel size in comparison to previous reports^{40-42,45}. During the in-situ test, the cell was repeatedly charged by a portable potentiostat (Gamry, Interface 1000E) to plate lithium until short circuit with intervals for imaging every 30 min. During the intervals, radiographic projections were captured while the sample was rotated through 180° . The detailed experimental setup is contained in the Experimental Sections. For simplicity, two lithium electrodes in the symmetrical cell were still named as “cathode” and “anode” according to the current direction. That is, the side which lithium plated into during charging is “anode”, and the other side is “cathode”.

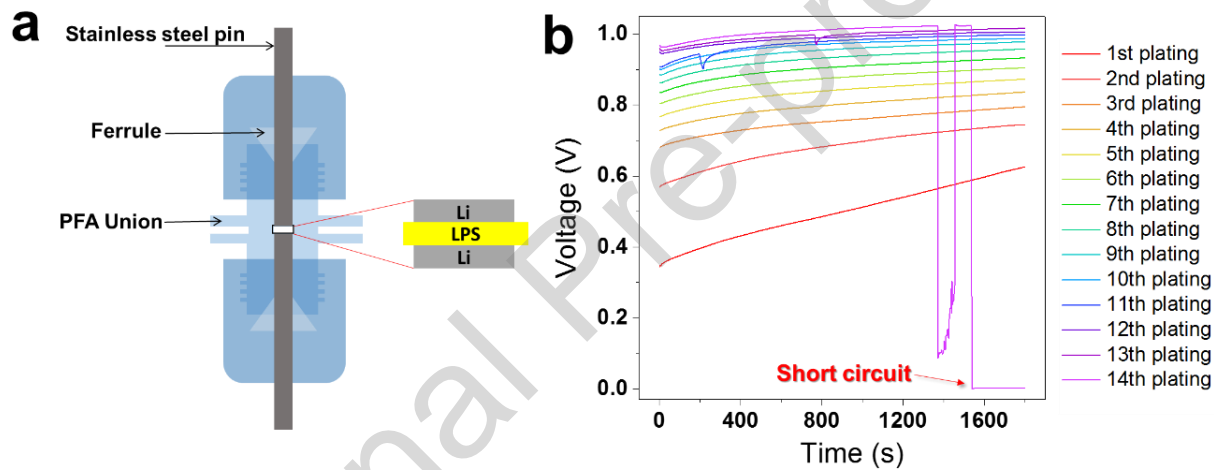


Fig 1. (a) Schematic of Swagelok cell; (b) Galvanostatic plating for 14 times until short-circuit

Fig 1b shows the electrochemical voltage curves at each plating step, where it can be observed that the polarization voltage gradually increased as the plating processed. This indicates the impedance of battery kept increasing during charging, attributed to the growing cracks inside the solid electrolytes⁴². Similar phenomena have also been observed in cycling LPS⁴⁵ and LAGP⁴². At the beginning of each step, the voltage slightly decreased due to relaxation during intervals. In the curve of 14th plating, the voltage abruptly decreased, quickly recovered and finally decreased to 0 V, which indicated a short circuit. Small drops in the 11th and 13th plating curves may have resulted from unstable connection between the sample and the wire of potentiostat after the sample was rotated repeatedly during tomography. In contrast to previous reports^{30,42,45}, the cell in this study was cycled until short-

circuit, so that a complete morphological evolution of LPS solid electrolyte during the whole electrochemical process was investigated. Here, the lithium was repeatedly plated (without stripping) with periodic pauses in the electrochemical process for X-ray tomographic data collection. Each interim plating is labelled as an independent step, and together a continuous process of lithium plating in the solid electrolyte can be observed.

By comparing the same slices in the LPS pellet after different plating times, the crack initiation and growth inside the solid electrolyte is clearly shown in Fig 2. Fig 2a illustrates the spatial locations of these orthogonal slices that are extracted from the 3D tomograms. Based on the Beer-Lambert Law, the gray level of X-ray CT projections is determined by the linear attenuation coefficient of the different constituent materials. Light regions in the slices (with high gray level) correspond to LPS, while darker regions correspond to the lithium electrode and cracks. As shown in Fig 2b and 2e, the original LPS pellet was intact without any detectable crack. After the 1st plating (Fig 2c, f), a few narrow cracks were generated at the LPS/Li anode interface. As shown in Fig 2f, they had not yet penetrated

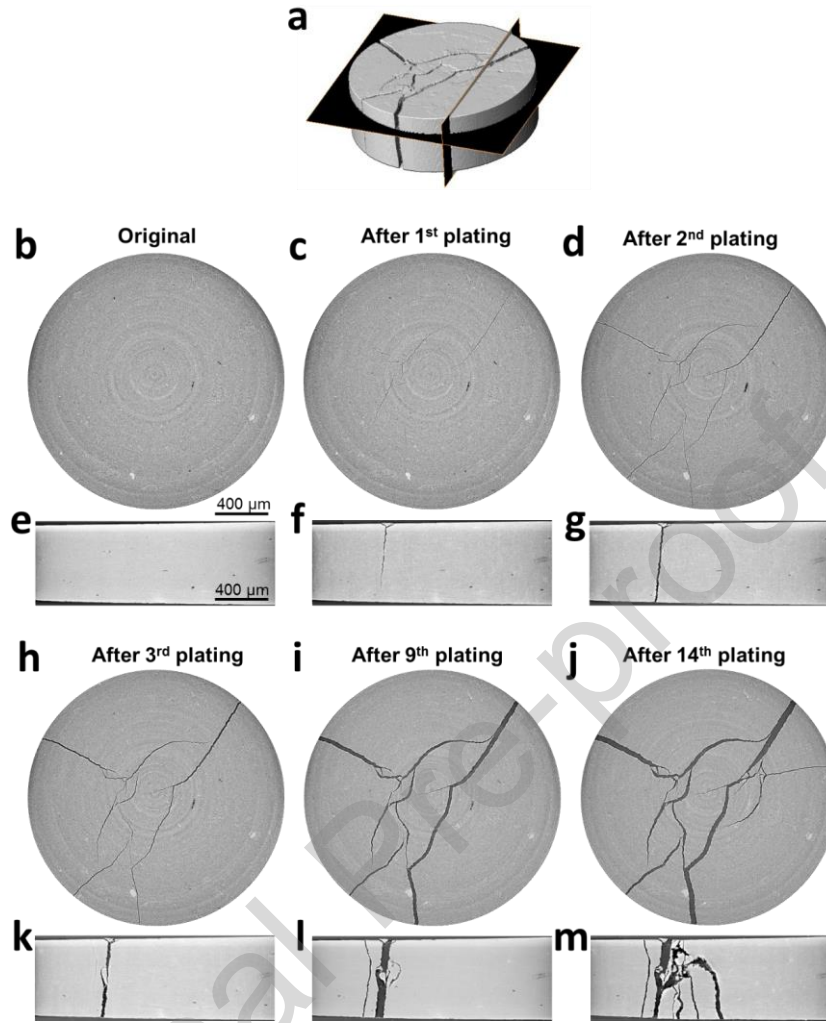


Fig 2. 2D orthogonal slices extracted from 3D tomogram as illustrated in (a, the 3D rendered volume of LPS pellet after 14th plating), comparing them at original state (b, e) and after 1st (c, f), 2nd (d, g), 3rd (h, k), 9th (i, l) and 14th (j, m) plating.

through the LPS pellet. The start point of crack had two small branches near the pellet surface; after two plating steps (shown in Fig 2d and g), cracks propagated in both lateral and vertical orientation, so that they reached the pellet edges and the cathode side. Subsequently, with more lithium plating in the following steps until short-circuit, cracks kept widening and growing into new branches, as shown in Fig 2h-m.

It is worth nothing that although the cracks had already penetrated through the solid electrolyte by the 2nd plating, the battery worked well with stable voltage curve (Fig 1b). This indicates that the crack reached the cathode ahead of the deposited lithium. The phenomenon will be analysed further in the following.

The 3D structures of cracks were reconstructed using a filtered back-projection algorithm, as shown in Fig 3a-c, so that the evolution of crack morphology was clearly revealed. Cracks were in the shape of thin sheets. At the early stage of crack growth, after the 1st plating (Fig 3a), thin-sheet cracks initiated from the LPS/Li anode interface, and subsequently propagated towards the cathode and extended laterally (Fig 3b-c). Meanwhile, they kept expanding and became wider, comparing Fig 3b with 3c. The sheet-like cracks were roughly perpendicular to the surface of LPS surface. The two small branches in the 2D slices (Fig 2f) near the LPS surface formed an approximate hemisphere in 3D,

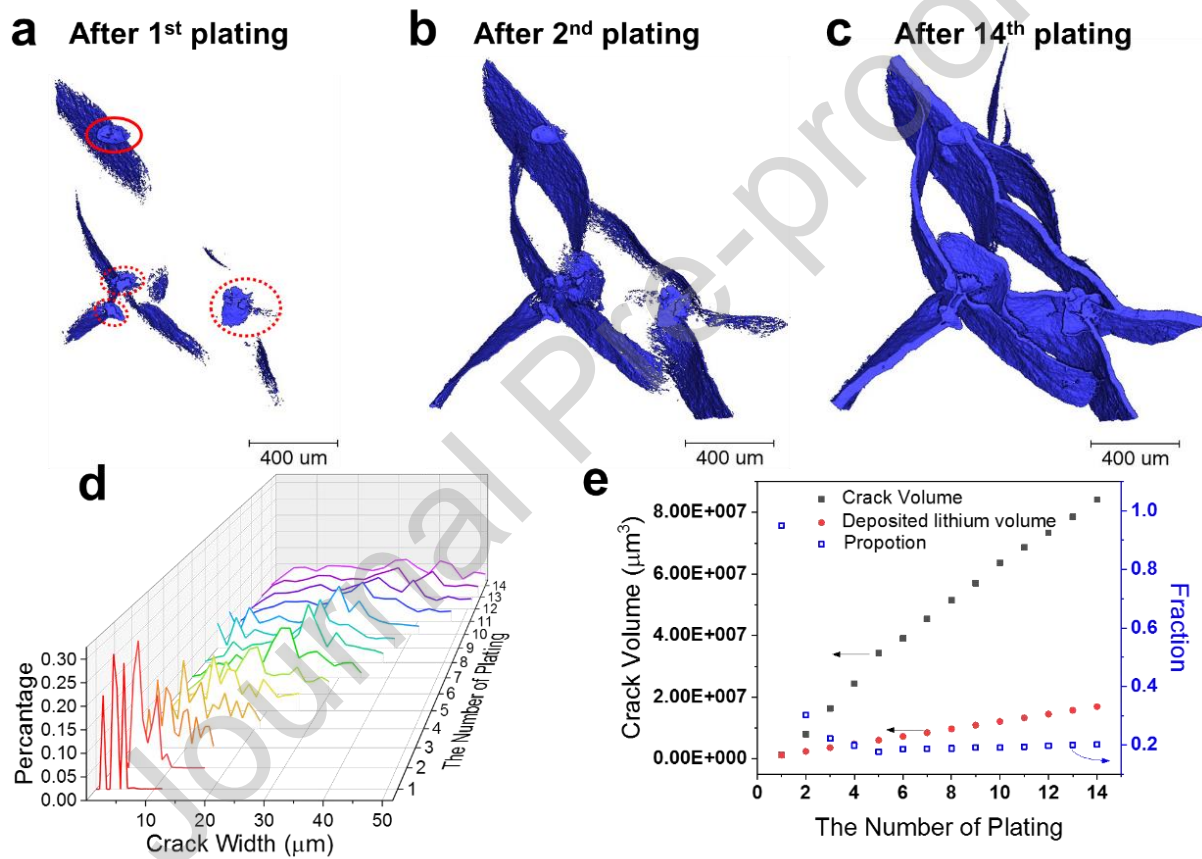


Fig 3. 3D rendering of cracks after 1st (a), 2nd (b) and 14th (c) plating; (d) the distribution of crack width after different plating times; (e) Plots showing the crack volume extracted from tomograms and the lithium volume calculated based on the transferred charge after different plating times

indicated by a red circle in Fig 3a and magnified in Fig S1. Another three similar features were identified near the LPS/ Li anode surface, as indicated by the red dotted circles. Note that these hemispheres first formed after the 1st plating (Fig 3a) and grew into thin sheets as

shown in Fig 2f, it is speculated to be the initiation positions of cracks in the solid electrolyte where the lithium first penetrated. Similar structures were also observed in oxide-based solid electrolytes³⁰ and solid polymer electrolytes³⁸, although their mechanical properties are different.

Next, cracks were quantified and analysed statistically in the series of tomographic images. The distribution of crack widths in each 3D tomogram was extracted and plotted in Fig 3d, and compared after different plating times. The primary crack width gradually and continuously increased from ca. 5 μm to 40 μm during the whole plating process until short circuit, which corresponded to the major and long cracks shown in Fig 3a-c. Additional small cracks generated with plating occupied a small proportion. This crack expansion/widening can be driven by two kinds of forces: the internal stress in LPS induced by the lithium propagation and the external stress from the battery case. Considering the pellet was intact before plating although it had already been assembled in the battery case (Fig 2b, 2e), the external stress itself was insufficient to break the LPS pellet. Therefore, the internal stress in LPS was the primary factor that caused the pellet fracture. In other words, cracks were driven by the lithium deposition, although the cracks alone did not directly cause cell failure, even though they penetrated the solid electrolyte and observably widened.

The volume of cracks after plating for different times was quantified and compared in Fig 3e. It continuously increased in an approximately linear fashion as the plating progressed. Based on the charge transferred in each plating step, the corresponding volume of lithium metal was calculated, assuming all transferred charge was used to deposit lithium. It was proportional to the plating time, indicated by the red dots in Fig 3e. It is noteworthy that only after the first plating, the volume of cracks are close to that of deposited lithium. In subsequent plating steps, the crack volume was increased much faster than the lithium volume indicating that cracks were only partially filled with lithium and had a great amounts of void-space inside. The volume ratio of lithium to cracks is calculated and shown by blue hollow boxes in Fig 3e. It dramatically dropped from 94.95 % after the 1st plating, to 30.19 % after the 2nd plating, and stabilized at about 20 % until short circuit. The LPS/Li interfaces remained straight and smooth and no substantial lithium was found to deposit there, as shown in Fig S2. Importantly, the partially filled cracks explains why the battery was not immediately short-circuited when cracks penetrated through LPS pellet: the plated lithium didn't always completely fill cracks or propagate simultaneously with them, indeed it

propagated much more slowly than the cracks considering the high speed of brittle fracture. Short circuiting only occurred when lithium grew and reached the counter electrode, after the 14th plating step in this case. As lithium started depositing and filling cracks from the LPS/Li anode interface, the part of cracks closer to the cathode side was speculated to be largely hollow in the early plating steps. This is the first time to the authors' knowledge that the volume fraction of Li plated within cracks has been quantified during the plating process. In previous modelling studies^{22,52} cracks have been generally regarded as fully filled with lithium, especially at the initiation stage of crack, so that lithium offered a driving force. In our result, the volume fraction of lithium within the cracks was also quite high at the initiation stage (after 1st plating), which is consistent with the modelling work. However, as plating proceeds, the subsequent decrease in volume fraction suggests a different mechanism in crack propagation compared with the early stage.

Line profiles of the grayscale value along a trajectory "ABC", as labelled by a red dotted line in Fig 4a, were tracked in the time-lapse tomograms. As shown in Fig 4b, the "BC" segment is used as a reference, and kept a stable grayscale of LPS at ca. 26000 a.u. (arbitrary unit) with small noise fluctuations, confirming a stable X-ray flux during the whole process. The "AB" segment had the same grayscale level after the 1st plating as cracks had not extended to this area at that time (Fig 2c). The grayscale dramatically dropped to around 22000 a.u. when a crack branch formed after the 2nd plating (Fig 2d), and maintained this level after the 3rd plating. It subsequently increased to ca. 24000 a.u. since the 4th plating and maintained the value until short circuit. Based on different attenuation coefficients, the lowest grayscale at 22000 a.u. corresponded to voids (air), while 24000 a.u. corresponded to lithium. Although it was difficult to distinguish the lithium and adjacent voids in cracks by visual inspection of raw 2D slices, their difference is resolved in grayscale in the high quality image obtained using a synchrotron-based coherent X-ray beam. This increase in grayscale during plating illustrates a filling process of lithium into cracks: the crack branch along "AB" was originally hollow (after the 2nd plating), but filled with lithium after the subsequent two plating steps (after the 4th plating). However, not all parts of cracks were filled with lithium. As shown in Fig 4c, the "DEF" trajectory along another crack branch showed a varied grayscale level after the 14th plating, which can be assigned to voids, lithium and LPS. The crack tip, around point "E" in the trajectory, was still largely voids after short circuit. The line profiles along another two branches, indicated as blue and yellow dotted lines in Fig 4a, were

shown and compared in Fig S3b. The wide branch in blue was almost full of lithium, while the narrow one in yellow was still largely hollow. It is suggested that the narrow and small crack branches that formed later tended to be hollow. The lithium filling process was also reflected in the line profile of a trajectory that was perpendicular to the cracks, as shown in Fig S3c. With the crack widening, the grayscale in the middle of the crack increased to the value of lithium, while near the crack walls it remained a relatively low value, suggesting the expanded space in the crack (at the crack walls) also tended to be hollow. The distribution of the unfilled space in crack branches confirmed the above analysis that cracks propagate quickly in the brittle LPS, but the lithium cannot fill in these spaces immediately.

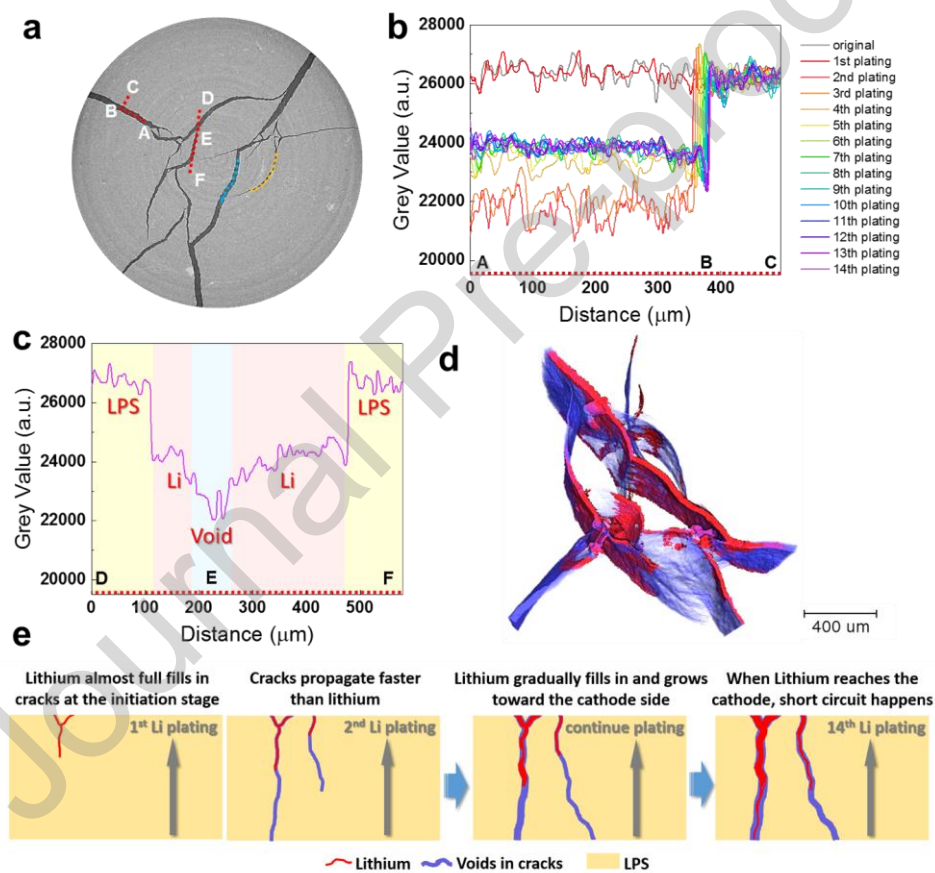


Fig 4. The line profile of grayscale along cracks as labelled in the slice after 14th plating (a); (b) comparing line profiles along the trajectory “ABC” during the whole plating process; (c) the line profile along the trajectory “DEF” after 14th plating in (a). (d) 3D distribution of lithium inside cracks after 14th plating, with lithium in red and voids in transparent blue. (e) Schematic illustration of lithium filling in cracks

Based on the different grayscale, the lithium with a grey value at ca. 24000 a.u. was threshold segmented from voids at ca. 22000 a.u. and its locations after the 14th plating is shown in Fig 4d. This image analysis step enabled segmentation of the LPS, voids and metallic Li; this was further corroborated by comparison of the segmented lithium volume, with the expected volume of deposited lithium calculated from the electrochemical data. Lithium filled the major cracks and reached the cathode at certain regions, although it was largely concentrated at the anode side. The small and narrow crack branches, that were formed or extended later, were rarely filled. It is the first time known to the authors that the distributions of lithium inside cracks in solid electrolytes have been resolved in such detail.

Combining the analysis on the filling ratio and the lithium distribution in cracks, the process of lithium growth during plating is schematically illustrated in Fig 4e and can be summarised as follows: after the 1st plating, the small and narrow cracks were almost fully filled with lithium that drove cracks to propagate. Then, the cracks extended rapidly and new branches formed after the 2nd plating, but left lots of unfilled spaces. The region adjacent to the anode side was largely filled with lithium, while the part nearer the cathode side was not. Subsequently, as more lithium deposited into the cracks, it filled more space within cracks and grew along cracks towards the cathode. In spite of more lithium deposited, the filling ratio still decreased a little overall, as calculated in Fig 3e, caused by a higher speed of crack propagation than lithium deposition. Considering the high brittleness of LPS, cracks can grow very fast, preceding lithium filling. Besides, the amount of deposited lithium based on the plating current was smaller than that needed to fully fill cracks. Consequently, the later extended space was largely hollow, resulting in a low filling ratio. This coupled process of crack expansion and lithium filling lasted until the 14th plating step, whereupon lithium in cracks finally reached the cathode side and the cell short-circuited where the filling ratio reached 20.14 % and lithium was still largely concentrated near the anode side. In general, the lithium deposition drove cracks to propagate, which was simultaneously influenced by the mechanical property of the solid electrolyte governed by the coupled electrochemical and mechanical behaviour of the system.

Additionally, after the cell was short-circuited, it was continuously imaged in-situ for another 1.5 h (that is until the 17th plating). As shown in Fig S4, the tomography of cracks and the lithium distribution had not changed since short circuit. This confirmed that a single external pressure from the battery case cannot cause the crack propagation. A voltage bias,

that is to say the electrochemical plating, is the prerequisite and incentive to both lithium plating and crack growth.

The distribution of lithium and voids confirms our analysis for the lag of short circuit, and provides more detail regarding the lithium filling process. In the following, the distribution of stress and strain and their evolution during plating is analysed further.

Although mechanical studies are a critical aspect of solid electrolyte research^{29,53}, uncertainties remain relating to the stress and strain distribution and its evolution during lithium dendrites growth. By performing digital volume correlation (DVC) analysis on the in-situ tomography datasets, 3D strain distributions inside the LPS pellet and their evolution during the whole plating process was obtained, as shown in Fig 5 and Video 1. Adjacent tomograms were compared and correlated to calculate the strains in every step of plating. In Fig 5a, the change of maximum normal strain in each plating stage is plotted. The strain was found to dramatically increase after the 2nd, 11th and 13th plating, but was relatively small and slightly decreased during the other plating steps. By extracting the same slice from the sample, normal strain distributions were mapped after the 1st, 2nd, 3rd, 10th, 11th, 12th, 13th and 14th plating, as shown in Fig 5b-i. The strains were coloured according to their value, and superimposed on raw greyscale images to show their positions relative to the cracks. Meanwhile, displacements around the cracks are shown by a matrix of arrows (magnification in Fig S5), in which colours correspond to the displacement magnitude and arrow directions indicate the orientation of displacement.

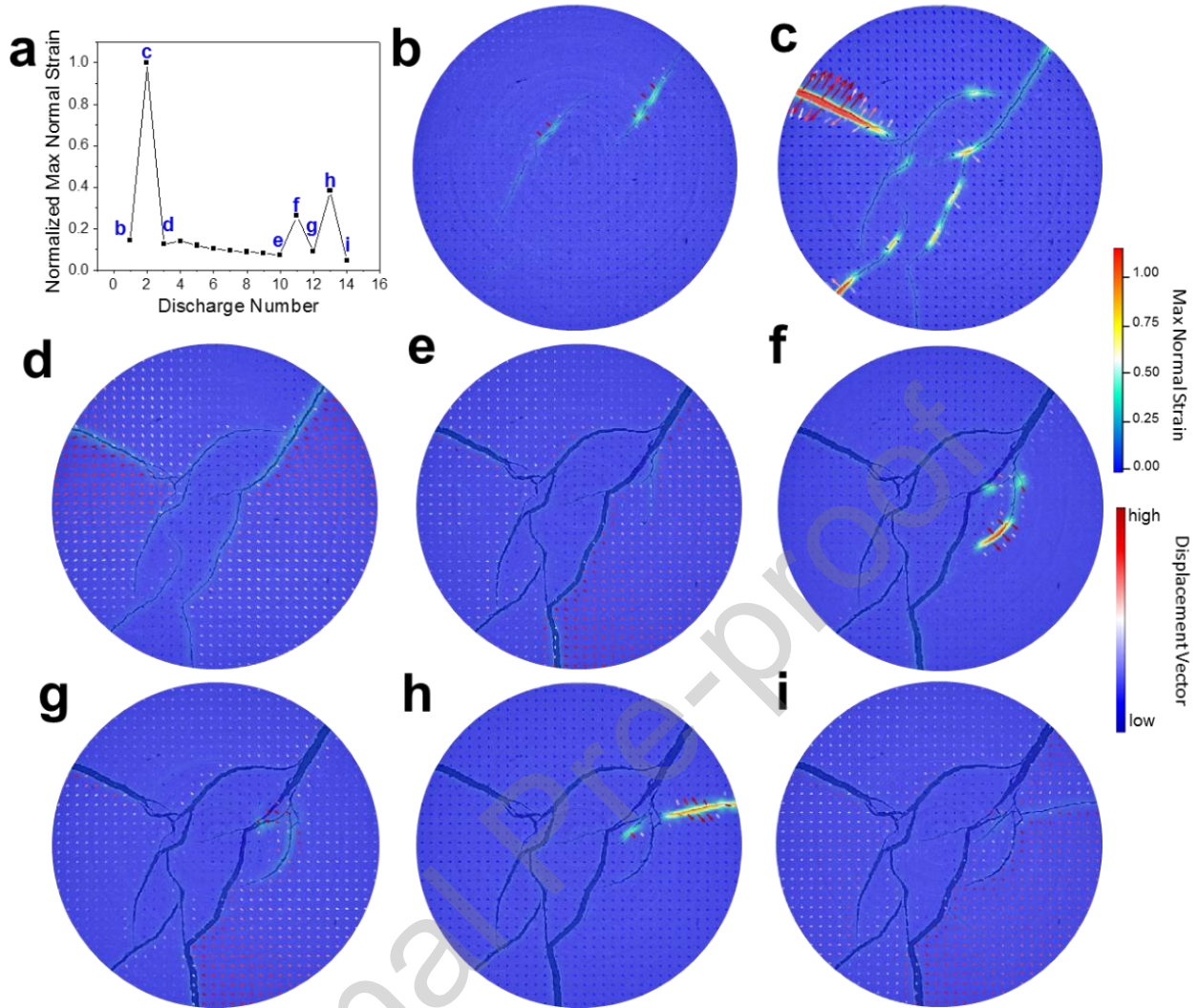


Fig 5. Evolution of normal strains during discharging. (a) Plot of maximum normal strain after different plating times; the normal strain distribution viewed at the same position of sample after 1st (b), 2nd (c), 3rd (d), 10th (e), 11th (f), 12th (g), 13th (h) and 14th (i) plating.

From Fig 5c, f and h, it is found that the large normal strains, which caused a sudden increase in Fig 5a, concentrated along the newly formed crack branches. They were quickly released in the next stage (Fig 5d, g, i). The strains remained small from 3rd to 10th plating (Fig 5a, d and e), as cracks only widened, without new branches forming. This indicates, at least in this case, that lateral crack growth is associated with larger normal strain than crack widening or opening. The small strains during crack opening remains concentrated along the cracks, and can be visualised clearly if the colormap in Fig 5 is re-scaled based on the individual images (Video 2). The hemispherical cracks near the anode interface also had large strains after the 1st plating, as the initiation positions of cracks (Fig S6). Shear strain has a

similar evolution trend, as shown in Video 3. The strain distribution is also displayed in the 3D iso-surface configuration during the whole plating process (Video 4).

From a mechanical perspective, the inorganic LPS solid electrolyte can be considered as a linear elastic solid¹⁷ that follows Hooke's law. The large strain area corresponds to the locations under high stress, and the increase and concentration of large strains along newly formed crack branches indicate that high stress forced cracks to propagate at these areas. Consequently, proportional to the stress, the adjacent LPS underwent large displacement, as indicated by the red arrows in Fig 5c, f and h. In this electrochemical plating process until short circuit, the stress mainly came from the lithium that continuously plated and grew into the solid electrolyte. As discussed previously, whilst the battery case also added external pressure to the cell, it was not the main cause. The almost fully-filled cracks after 1st plating (Fig 4a) induced the largest stress and strain in the subsequent 2nd plating (Fig 5a, 5c). Once cracks penetrated the solid electrolyte after 2nd plating as brittle fracture occurred, stress was much decreased but kept concentrating along cracks to make them wider (Fig 5 and S1). In some areas, the local stress and strain that were relatively higher, c.f. the 11th (Fig 5f) and 13th plating (Fig 5h), induced new branches. Additionally, the fabrication process (cold press) may cause additional stresses to arise inside the pellet, which could have also played a role in crack propagation by interacting with other stresses (for example from the lithium and the battery case) in a complex fashion. More investigation is needed to clarify these phenomena further.

Moreover, as indicated by the matrix of arrows in Fig 5b-i, the LPS fragments were observed to move apart and separate into several segments during the whole process. When cracks opened in Fig 5d-e, the displacement of the LPS fragment was larger near the cracks and became smaller further away from cracks, as indicated by the colour of arrows changing from red to white. This means the LPS material was slightly compressed at the regions near cracks. At the micro scale, plastic deformation may have existed, and could be considered in future modelling studies. Additionally, as shown in Fig 5c, 5f and 5h, crack widening was impaired, and nearly stopped in instances when new branches were growing. This is the first time known to authors that the stress and strain evolution in a solid electrolyte has been resolved in detail; based on this, the whole process of lithium plating is comprehensively analysed from morphological, electrochemical and mechanical perspectives.

Considering crack initiation could ultimately nucleate at atomic length scales, cracks may present below the image resolution here. With the further development of CT facilities, more studies (outside of the scope of the current work) could be made at a higher resolution, so the interaction between cracks and lithium penetrations can be resolved further.

Conclusion

In this work, the 3D morphological evolution of cracks with deposited lithium inside a LPS solid electrolyte was tracked by in-situ X-ray CT during a repetitive plating process until short circuit. Utilizing high flux synchrotron X-ray and a bespoke cell design, spatial and temporal resolution was notably improved; meanwhile the integrity of the sample was well preserved without any disturbance or movement. Cracks in the shape of a thin sheet initiated from LPS/Li anode interface and grew through the pellet after the 2nd plating, but the cell performed well until short circuit occurred after the 14th plating. Through image processing and quantitative statistics, the crack width was found to expand from ca. 5 μm to 40 μm ; and crack volume increased in an approximate linear fashion as the plating progressed. By calculating the amount of deposited lithium in the plating process, the lithium was found to partially fill cracks with a filling ratio dropping from 94.95 % after the 1st plating to ca. 20 % after the 4th plating. Through tracking the line profile of grayscale along cracks, the lithium filling process was revealed which occurred later than crack generation; narrow crack branches and tips which formed afterward remained largely hollow. Based on different grayscale levels, the lithium distribution after short circuit was segmented and obtained in 3D. The whole process of lithium deposition and crack propagation was analysed in detail considering the coupled electrochemical and mechanical effects. The lag of short circuit resulted from a partial and slow filling process of lithium into cracks. Finally, by DVC analysis, the stress and strain in LPS were found to aggregate along cracks, and significantly increased after lithium filling in the 1st plating and sometimes at crack branches in subsequent steps, which forced cracks to propagate in these areas.

To the authors' knowledge, this is the first time that the evolution of cracks and lithium in solid electrolytes during a whole plating process until short circuit, together with corresponding stress and strain, have been revolved in such detail. They are comprehensively analysed from morphological, electrochemical and mechanical perspectives to inform the mechanism of lithium penetrating the solid electrolyte. These results enrich the basic

understanding of lithium propagation in solid electrolytes, and would enlighten relevant modelling or experimental studies on this critical topic to accelerate the development of solid state batteries.

Experimental Sections

Cell Fabrication:

Li₃PS₄ powder (MSE Supplies LLC, USA) was cold pressed in an Ar-filled glove box, into a pellet with a thickness ca. 0.6 mm, a diameter of ca. 2 mm. The symmetrical Li/LPS/Li cell was assembled in modified PFA Swagelok straight unions (PFA-220-6, Swagelok, UK), with ca. 0.9 mm thick lithium foil pressing onto both sides of the LPS pellet.

Synchrotron X-ray tomography:

In-situ experiments were conducted on the I13-2 Diamond-Manchester Branchline at Diamond Light Source (Harwell, UK). The X-ray beam used for imaging was a filtered pink beam with an energy range of 18 – 24 keV. The spectral mean energy was 22.3 keV. The spectrum was generated by using an ID gap of 5.0 mm and the following filters with respective thicknesses t : pyrolytic graphite, $t=1.34$ mm; aluminium, $t=2.1$ mm; silver, $t=35$ μm ; palladium, $t=42$ μm . The detector was a PCO.Edge 5.5 detector with 4 \times Objective lens for 8 \times total optical magnification, resulting in a pixel size of ca. 0.8 μm and a field of view of ca. 2.1 \times 1.8 mm. During each tomographic acquisition, a total of 2400 projections were collected over 180 $^\circ$ angular range with an exposure time of 0.2 s per frame. The projection datasets were reconstructed by a parallel beam filtered back projection algorithm. The cell was stopped plating during imaging to ensure a consistent state of charge through the scan.

The tomograms were processed in Avizo (Thermo Fisher Scientific, Waltham, Massachusetts, USA) through filtering and segmentation. The region of the LPS pellet was isolated from the whole volume. The width of cracks was quantified and counted in each tomogram to get its distribution. The volume of cracks was extracted and compared at different plating times.

Electrochemistry:

Between each tomographic acquisition, the cell was charged with a potentiostat (Interface 1000E, Gamry Instruments) at a constant current density of 0.15 mA cm^{-2} at room temperature. It was kept on the beamline sample stage without any movement and directly connected to the potentiostat by wires. The beam shutter was automatically closed during each charge/plating step.

DVC analysis:

DVC analysis was carried out in DaVis (V10.1, LaVision, Germany) on the in-situ CT tomograms to retrieve the displacement and strain in LPS pellet. The tomograms were cropped to remove empty volume outside of LPS pellet. A multi-pass scheme was used to correlate volume by sub-volumes of 64^3 , 48^3 , 32^3 and 16^3 voxels with a 75 % overlap. Each tomogram was sorted by plating numbers and correlated to its predecessor. Thus the resulting displacement and strain field describes changes between tomograms after adjacent plating times. Vectors were coloured based on the displacement range in each image. The strains were coloured based on their magnitude among all images in Fig 5 and Video 1. While the colour was rescaled based on individual image in Video 2.

Acknowledgement

The authors acknowledge the financial support from the Faraday Institution All-Solid-State Batteries with Li Anode (EP/S003053/1, FIRG007). P.R.S. acknowledges the support of The Royal Academy of Engineering (CIET178/59). The authors acknowledge the Diamond Light Source for synchrotron beam time on the Diamond-Manchester Branchline (I13-2) under experiment number MG22198-1.

References

- 1 Monroe, C. & Newman, J. The Impact of Elastic Deformation on Deposition Kinetics at Lithium/Polymer Interfaces. *Journal of The Electrochemical Society* **152**, A396-A404, doi:10.1149/1.1850854 (2005).
- 2 Ren, Y., Shen, Y., Lin, Y. & Nan, C. W. Microstructure Manipulation for Enhancing the Resistance of Garnet-Type Solid Electrolytes to "Short Circuit" by Li Metal Anodes. *ACS Appl Mater Interfaces* **11**, 5928-5937, doi:10.1021/acsami.8b17954 (2019).

- 3 Sharafi, A., Haslam, C. G., Kerns, R. D., Wolfenstine, J. & Sakamoto, J. Controlling and correlating the effect of grain size with the mechanical and electrochemical properties of Li₇La₃Zr₂O₁₂ solid-state electrolyte. *J. Mater. Chem. A* **5**, 21491-21504, doi:10.1039/c7ta06790a (2017).
- 4 Nagao, M. *et al.* In situ SEM study of a lithium deposition and dissolution mechanism in a bulk-type solid-state cell with a Li₂S-P₂S₅ solid electrolyte. *Phys Chem Chem Phys* **15**, 18600-18606, doi:10.1039/c3cp51059j (2013).
- 5 Kim, S. H. *et al.* In situ observation of lithium metal plating in a sulfur-based solid electrolyte for all-solid-state batteries. *Journal of Materials Chemistry A* **7**, 13650-13657, doi:10.1039/c9ta02614b (2019).
- 6 Dolle, M., Sannier, L., Beaudoin, B., Trentin, M. & Tarascon, J. M. Live scanning electron microscope observations of dendritic growth in lithium/polymer cells. *Electrochem. Solid State Lett.* **5**, A286-A289, doi:10.1149/1.1519970 (2002).
- 7 Harry, K. J., Liao, X., Parkinson, D. Y., Minor, A. M. & Balsara, N. P. Electrochemical Deposition and Stripping Behavior of Lithium Metal across a Rigid Block Copolymer Electrolyte Membrane. *Journal of The Electrochemical Society* **162**, A2699-A2706, doi:10.1149/2.0321514jes (2015).
- 8 Tan, S.-J., Zeng, X.-X., Ma, Q., Wu, X.-W. & Guo, Y.-G. Recent Advancements in Polymer-Based Composite Electrolytes for Rechargeable Lithium Batteries. *Electrochemical Energy Reviews* **1**, 113-138, doi:10.1007/s41918-018-0011-2 (2018).
- 9 Han, X. *et al.* Negating interfacial impedance in garnet-based solid-state Li metal batteries. *Nat Mater* **16**, 572-579, doi:10.1038/nmat4821 (2017).
- 10 Zhou, W. *et al.* Polymer lithium-garnet interphase for an all-solid-state rechargeable battery. *Nano Energy* **53**, 926-931, doi:10.1016/j.nanoen.2018.09.004 (2018).
- 11 Gao, Y. *et al.* Salt-Based Organic-Inorganic Nanocomposites: Towards A Stable Lithium Metal/Li₁₀ GeP₂ S₁₂ Solid Electrolyte Interface. *Angew Chem Int Ed Engl* **57**, 13608-13612, doi:10.1002/anie.201807304 (2018).
- 12 Tan, S. J. *et al.* Nitriding-Interface-Regulated Lithium Plating Enables Flame-Retardant Electrolytes for High-Voltage Lithium Metal Batteries. *Angew Chem Int Ed Engl* **58**, 7802-7807, doi:10.1002/anie.201903466 (2019).
- 13 Xu, S. *et al.* All-in-one lithium-sulfur battery enabled by a porous-dense-porous garnet architecture. *Energy Storage Materials* **15**, 458-464, doi:10.1016/j.ensm.2018.08.009 (2018).
- 14 Zhang, Z. *et al.* All-in-one improvement toward Li₆PS₅Br-Based solid electrolytes triggered by compositional tune. *Journal of Power Sources* **410-411**, 162-170, doi:10.1016/j.jpowsour.2018.11.016 (2019).

- 15 Motoyama, M., Ejiri, M. & Iriyama, Y. Modeling the Nucleation and Growth of Li at Metal Current Collector/LiPON Interfaces. *Journal of The Electrochemical Society* **162**, A7067-A7071, doi:10.1149/2.0051513jes (2015).
- 16 Raj, R. & Wolfenstine, J. Current limit diagrams for dendrite formation in solid-state electrolytes for Li-ion batteries. *Journal of Power Sources* **343**, 119-126, doi:10.1016/j.jpowsour.2017.01.037 (2017).
- 17 Shishvan, S. S., Fleck, N. A., McMeeking, R. M. & Deshpande, V. S. Dendrites as climbing dislocations in ceramic electrolytes: Initiation of growth. *Journal of Power Sources* **456**, 227989, doi:10.1016/j.jpowsour.2020.227989 (2020).
- 18 Krauskopf, T. *et al.* Lithium-Metal Growth Kinetics on LLZO Garnet-Type Solid Electrolytes. *Joule* **3**, 2030-2049, doi:10.1016/j.joule.2019.06.013 (2019).
- 19 Han, F. *et al.* High electronic conductivity as the origin of lithium dendrite formation within solid electrolytes. *Nature Energy* **4**, 187-196, doi:10.1038/s41560-018-0312-z (2019).
- 20 Golozar, M. *et al.* In Situ Scanning Electron Microscopy Detection of Carbide Nature of Dendrites in Li-Polymer Batteries. *Nano Lett* **18**, 7583-7589, doi:10.1021/acs.nanolett.8b03148 (2018).
- 21 Manalastas, W. *et al.* Mechanical failure of garnet electrolytes during Li electrodeposition observed by in-operando microscopy. *Journal of Power Sources* **412**, 287-293, doi:10.1016/j.jpowsour.2018.11.041 (2019).
- 22 Porz, L. *et al.* Mechanism of Lithium Metal Penetration through Inorganic Solid Electrolytes. *Advanced Energy Materials* **7**, doi:10.1002/aenm.201701003 (2017).
- 23 Wu, B. *et al.* The role of the solid electrolyte interphase layer in preventing Li dendrite growth in solid-state batteries. *Energy & Environmental Science* **11**, 1803-1810, doi:10.1039/c8ee00540k (2018).
- 24 Ren, Y., Shen, Y., Lin, Y. & Nan, C.-W. Direct observation of lithium dendrites inside garnet-type lithium-ion solid electrolyte. *Electrochemistry Communications* **57**, 27-30, doi:10.1016/j.elecom.2015.05.001 (2015).
- 25 Pesci, Federico M. *et al.* Elucidating the role of dopants in the critical current density for dendrite formation in garnet electrolytes. *Journal of Materials Chemistry A* **6**, 19817-19827, doi:10.1039/c8ta08366e (2018).
- 26 Marbella, L. E. *et al.* ⁷Li NMR Chemical Shift Imaging To Detect Microstructural Growth of Lithium in All-Solid-State Batteries. *Chemistry of Materials* **31**, 2762-2769, doi:10.1021/acs.chemmater.8b04875 (2019).
- 27 Li, Q. *et al.* In-situ visualization of lithium plating in all-solid-state lithium-metal battery. *Nano Energy* **63**, 103895, doi:10.1016/j.nanoen.2019.103895 (2019).

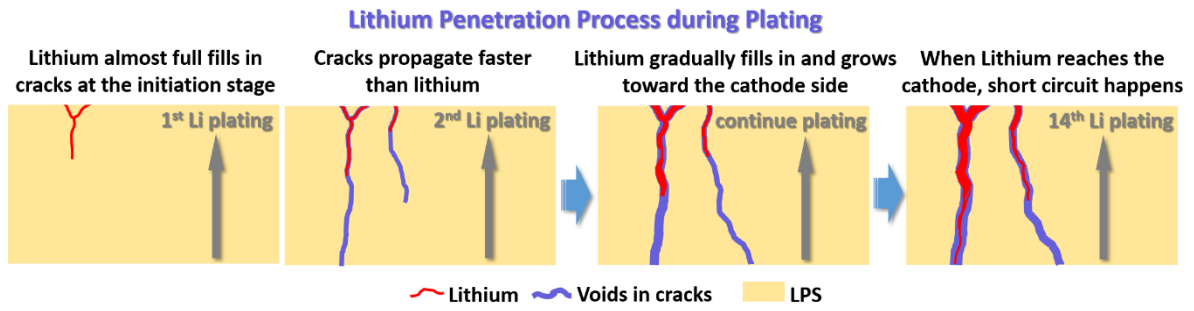
- 28 Muramatsu, H., Hayashi, A., Ohtomo, T., Hama, S. & Tatsumisago, M. Structural change of Li₂S–P₂S₅ sulfide solid electrolytes in the atmosphere. *Solid State Ionics* **182**, 116-119, doi:10.1016/j.ssi.2010.10.013 (2011).
- 29 Mangani, L. R. & Villevieille, C. Mechanical vs. chemical stability of sulphide-based solid-state batteries. Which one is the biggest challenge to tackle? Overview of solid-state batteries and hybrid solid state batteries. *Journal of Materials Chemistry A* **8**, 10150-10167, doi:10.1039/d0ta02984j (2020).
- 30 Kazyak, E. *et al.* Li Penetration in Ceramic Solid Electrolytes: Operando Microscopy Analysis of Morphology, Propagation, and Reversibility. *Matter* **2**, 1025-1048, doi:10.1016/j.matt.2020.02.008 (2020).
- 31 Kim, S. *et al.* The Role of Interlayer Chemistry in Li - Metal Growth through a Garnet - Type Solid Electrolyte. *Advanced Energy Materials* **10**, 1903993, doi:10.1002/aenm.201903993 (2020).
- 32 Wood, V. X-ray tomography for battery research and development. *Nature Reviews Materials* **3**, 293-295, doi:10.1038/s41578-018-0053-4 (2018).
- 33 Pasta, M. *et al.* 2020 roadmap on solid-state batteries. *Journal of Physics: Energy* **2**, doi:10.1088/2515-7655/ab95f4 (2020).
- 34 Pietsch, P. & Wood, V. X-Ray Tomography for Lithium Ion Battery Research: A Practical Guide. *Annual Review of Materials Research* **47**, 451-479, doi:10.1146/annurev-matsci-070616-123957 (2017).
- 35 Eastwood, D. S. *et al.* Three-dimensional characterization of electrodeposited lithium microstructures using synchrotron X-ray phase contrast imaging. *Chem Commun (Camb)* **51**, 266-268, doi:10.1039/c4cc03187c (2015).
- 36 Sun, F. *et al.* Morphological Evolution of Electrochemically Plated/Stripped Lithium Microstructures Investigated by Synchrotron X-ray Phase Contrast Tomography. *ACS Nano* **10**, 7990-7997, doi:10.1021/acsnano.6b03939 (2016).
- 37 Sun, F. *et al.* Correlating Morphological Evolution of Li Electrodes with Degrading Electrochemical Performance of Li/LiCoO₂ and Li/S Battery Systems: Investigated by Synchrotron X-ray Phase Contrast Tomography. *ACS Energy Letters* **3**, 356-365, doi:10.1021/acsenergylett.7b01254 (2018).
- 38 Harry, K. J., Hallinan, D. T., Parkinson, D. Y., MacDowell, A. A. & Balsara, N. P. Detection of subsurface structures underneath dendrites formed on cycled lithium metal electrodes. *Nat Mater* **13**, 69-73, doi:10.1038/nmat3793 (2014).
- 39 Kasemchainan, J. *et al.* Critical stripping current leads to dendrite formation on plating in lithium anode solid electrolyte cells. *Nature Materials*, doi:10.1038/s41563-019-0438-9 (2019).

- 40 Shen, F., Dixit, M. B., Xiao, X. & Hatzell, K. B. Effect of Pore Connectivity on Li Dendrite Propagation within LLZO Electrolytes Observed with Synchrotron X-ray Tomography. *ACS Energy Letters* **3**, 1056-1061, doi:10.1021/acsenergylett.8b00249 (2018).
- 41 Zhang, W. *et al.* (Electro)chemical expansion during cycling: monitoring the pressure changes in operating solid-state lithium batteries. *Journal of Materials Chemistry A* **5**, 9929-9936, doi:10.1039/c7ta02730c (2017).
- 42 Tippens, J. *et al.* Visualizing Chemomechanical Degradation of a Solid-State Battery Electrolyte. *ACS Energy Letters* **4**, 1475-1483, doi:10.1021/acsenergylett.9b00816 (2019).
- 43 Rau, C., Wagner, U., Pešić, Z. & De Fanis, A. Coherent imaging at the Diamond beamline I13. *physica status solidi (a)* **208**, 2522-2525, doi:10.1002/pssa.201184272 (2011).
- 44 Rau, C. Imaging with Coherent Synchrotron Radiation: X-ray Imaging and Coherence Beamline (I13) at Diamond Light Source. *Synchrotron Radiation News* **30**, 19-25, doi:10.1080/08940886.2017.1364530 (2017).
- 45 Seitzman, N. *et al.* Toward All-Solid-State Lithium Batteries: Three-Dimensional Visualization of Lithium Migration in β -Li₃PS₄ Ceramic Electrolyte. *Journal of The Electrochemical Society* **165**, A3732-A3737, doi:10.1149/2.0301816jes (2018).
- 46 Madsen, K. E. *et al.* Direct Observation of Interfacial Mechanical Failure in Thiophosphate Solid Electrolytes with Operando X - Ray Tomography. *Advanced Materials Interfaces* **7**, doi:10.1002/admi.202000751 (2020).
- 47 Sun, F. *et al.* Visualizing the morphological and compositional evolution of the interface of InLi-anode|thio-LISION electrolyte in an all-solid-state Li-S cell by in operando synchrotron X-ray tomography and energy dispersive diffraction. *Journal of Materials Chemistry A* **6**, 22489-22496, doi:10.1039/c8ta08821g (2018).
- 48 Haas, R. *et al.* Practical Implications of Using a Solid Electrolyte in Batteries with a Sodium Anode: A Combined X - Ray Tomography and Model - Based Study. *Energy Technology* **7**, doi:10.1002/ente.201801146 (2019).
- 49 Spencer Jolly, D. *et al.* Sodium/Na β '' Alumina Interface: Effect of Pressure on Voids. *ACS Applied Materials & Interfaces* **12**, 678-685, doi:10.1021/acsaami.9b17786 (2019).
- 50 Rees, G. J. *et al.* Imaging Sodium Dendrite Growth in All-Solid-State Sodium Batteries Using (23) Na T2 -Weighted Magnetic Resonance Imaging. *Angew Chem Int Ed Engl*, doi:10.1002/anie.202013066 (2020).
- 51 Tan, C. *et al.* Evolution of Electrochemical Cell Designs for In-Situ and Operando 3D Characterization. *Materials (Basel)* **11**, 2157, doi:10.3390/ma11112157 (2018).

- 52 Klinsmann, M., Hildebrand, F. E., Ganser, M. & McMeeking, R. M. Dendritic cracking in solid electrolytes driven by lithium insertion. *Journal of Power Sources* **442**, 227226, doi:10.1016/j.jpowsour.2019.227226 (2019).
- 53 Wang, P. *et al.* Electro–Chemo–Mechanical Issues at the Interfaces in Solid - State Lithium Metal Batteries. *Advanced Functional Materials* **29**, 1900950, doi:10.1002/adfm.201900950 (2019).

Journal Pre-proof

Graphical abstract



Journal Pre-proof

CRediT author statement

Shuai Hao: Conceptualization, Investigation, Writing–Original Draft. **Sohrab R. Daemi:** Investigation, Writing-Review & Editing. **Thomas M. M. Heenan:** Investigation, Writing-Review & Editing. **Wenjia Du:** Investigation, Writing-Review & Editing. **Chun Tan:** Investigation, Writing-Review & Editing. **Malte Storm:** Investigation, Software, Writing-Review & Editing. **Christoph Rau:** Investigation, Writing-Review & Editing. **Dan J. L. Brett:** Writing-Review & Editing. **Paul R. Shearing:** Conceptualization, Supervision, Writing-Review & Editing.

Journal Pre-proof

Declaration of interests

The authors declare that they have no known competing financial interests or personal relationships that could have appeared to influence the work reported in this paper.

The authors declare the following financial interests/personal relationships which may be considered as potential competing interests:

Journal Pre-proof

Highlights

1. The 3D morphological evolution of cracks and deposited lithium in a solid state battery was tracked by in-situ X-ray CT under high resolution 0.8 μm during a repetitive plating process until short circuit.
2. Lithium only partially filled the cracks, and propagated more slowly than the cracks resulting in a lag of short circuit.
3. The lithium filling ratio dramatically dropped from 94 % to ca. 20 % during plating, primarily due to the high speed of crack growth.
4. Stress and strain in the solid electrolyte aggregated along the cracks and their branches, forcing cracks to propagate in these areas.

Journal Pre-proof